WALL FUNCTIONS FOR ARBITRARILY ROUGH SURFACES WITH APPLICATION TO SEDIMENT MORPHODYNAMICS

David D. Apsley
School of Mechanical, Aerospace and Civil Engineering,
University of Manchester
PO Box 88, Manchester, M60 1QD, England
d.apsley@manchester.ac.uk

ABSTRACT

This paper describes: (1) a wall function for arbitrary surface roughness, with parameters determined as functions of roughness by imposing high-order consistency with the log law; (2) implementation of sediment morphodynamics in a 3-d RANS solver, with modifications for large slopes and arbitrary bed orientation. The wall function is validated for 2-equation and differential-stress closures in rough-wall pipe flow. Simulations of scour and deposition in a channel bend and of the evolution of sand mounds are described.

INTRODUCTION

Wall functions are used in CFD calculations of turbulent flow to accommodate the rapidly-varying flow near solid boundaries without an unacceptably-large number of grid cells. There are many situations where the surface roughness is intermediate between hydraulically-smooth and hydraulically-rough, and it is desirable to have a single wall function that can accommodate arbitrary roughness.

The present work was motivated by the application of CFD to experiments on sediment morphodynamics. Because sediment transport is driven by the fluid stress on the boundary, a good prediction of the wall stress is vital.

The following sections describe a wall function for arbitrary surface roughness, followed by implementation of sediment morphodynamics within a 3-d, finite-volume, RANS solver. Application of these to scour in a channel bend and to the evolution of sand mounds is then shown.

THE WALL FUNCTION

Main Elements

In a cell-centred finite-volume calculation of incompressible flow without heat transfer (Figure 1) a wall function must provide the following:

- for the mean-velocity equations – the wall shear stress τ_w;
- for the turbulent-kinetic-energy or Reynolds-stress equations – the *cell-averaged* production, $P_{av}^{(k)}$, and dissipation, ε_{av};
- for the dissipation equation – the value of dissipation ε at the near-wall node.

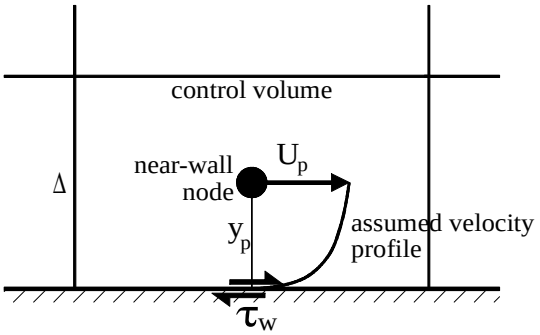

Figure 1: Near-wall cell.

The present model is related to that of Craft et al. (2006) with extension to rough walls by Suga et al. (2006). It shares with these works the following features.

1. The model uses a velocity scale based on turbulent kinetic energy at the near-wall node:
$$\tilde{u}_\tau = C_\mu^{1/4} k_P^{1/2} \qquad (1)$$
rather than the actual friction velocity $u_\tau = \sqrt{\tau_w / \rho}$. The two are equal in the log-law region, but $\tilde{u}_\tau$ provides a more appropriate scale near separation/reattachment points. In wall units, heights are then non-dimensionalised using $\tilde{u}_\tau$:
$$y^+ = y\tilde{u}_\tau / \nu \qquad (2)$$
2. A mean-velocity profile is derived from an assumed total-viscosity profile
$$\nu_{total} \equiv \nu + \nu_t = \nu + \max\{0, \kappa\tilde{u}_\tau (y - y_v)\} \qquad (3)$$
where κ (= 0.41) is von Kármán's constant.

3. The zero-eddy-viscosity height in wall units, y_v^+, is a function of k_s^+, where k_s is the Nikuradse roughness.

However, the present work differs from earlier authors in two important respects.

4. It adopts a different functional formulation (based on stronger asymptotic adherence to the log law) for the zero-eddy-viscosity height y_v;
5. There is a different assumed dissipation profile:

$$\varepsilon = \begin{cases} \dfrac{\tilde{u}_\tau^3}{\kappa(y - y_d)}, & y \ge y_\varepsilon \\ \varepsilon_w, & y \le y_\varepsilon \end{cases} \tag{4}$$

where ε is continuous at y_ε and both y_d and y_ε are functions of roughness.

Mean-Velocity Profile and Effective Wall Viscosity

The mean-velocity profile derived from a constant-stress assumption ($\tau = \tau_w$) and the eddy viscosity (3) can be written as

$$\frac{U}{\tilde{u}_\tau} = \frac{\tau_w}{\rho \tilde{u}_\tau^2} \times \begin{cases} y^+, & y^+ \le y_v^+ \\ y_{v0}^+ + \dfrac{1}{\kappa} \ln\left[\dfrac{1+\kappa(y^+ - y_v^+)}{1+\kappa(y_{v0}^+ - y_v^+)}\right], & y^+ \ge y_v^+ \end{cases} \tag{5}$$

where $y_{v0}^+ = \max\{y_v^+, 0\}$. Since the desired output of the wall function is τ_w in terms of U_p, not vice-versa, the velocity/stress relationship is implemented via an effective wall viscosity $\nu_{eff,wall}$ such that

$$\tau_w = \rho \nu_{eff,wall} \frac{U_p}{y_p} \tag{6}$$

The Zero-Eddy-Viscosity Height, y_v

y_v is determined by enforcing high-order consistency with the log law. In the log-law region, $\tau_w = \rho \tilde{u}_\tau^2$. (5) then gives (in the case where $y_v^+ > 0$):

$$\begin{aligned} U^+ &= y_v^+ + \frac{1}{\kappa} \ln[1 + \kappa(y^+ - y_v^+)] \\ &= \frac{1}{\kappa} \ln y^+ + \left(y_v^+ + \frac{1}{\kappa} \ln \kappa \right) + O\left(\frac{1}{y^+}\right) \end{aligned} \tag{7}$$

Comparing this with the log law for arbitrary roughness:

$$U^+ = \frac{1}{\kappa} \ln y^+ + B(k_s^+) \tag{8}$$

gives

$$y_v^+ = B - \frac{1}{\kappa} \ln \kappa \qquad (\text{if } B - \frac{1}{\kappa} \ln \kappa \ge 0) \tag{9}$$

For sufficiently large roughness the RHS of (9) is negative and a similar analysis leads to

$$y_v^+ = \frac{1}{\kappa}\left(1 - e^{-\kappa\left(B - \frac{1}{\kappa} \ln \kappa\right)}\right) \qquad (\text{if } B - \frac{1}{\kappa} \ln \kappa \le 0) \tag{10}$$

The zero-eddy-viscosity height y_v is then fully-prescribed once the roughness-dependent function B is specified. Simulation of fully-developed pipe flow leads to

$$B = 8 - \frac{1}{\kappa} \ln(k_s^+ + 3.152) \tag{11}$$

the constants being chosen to give typical smooth- and rough-wall limits, $B = 5.2$ and $B = 8 - (1/\kappa)\ln(k_s^+)$ respectively. y_v^+ is plotted as a function of k_s^+ in Figure 2. The smooth-wall value of y_v^+ is 7.37, whilst the viscous sublayer is destroyed (i.e. $y_v^+ = 0$) when $k_s^+ = 62$.

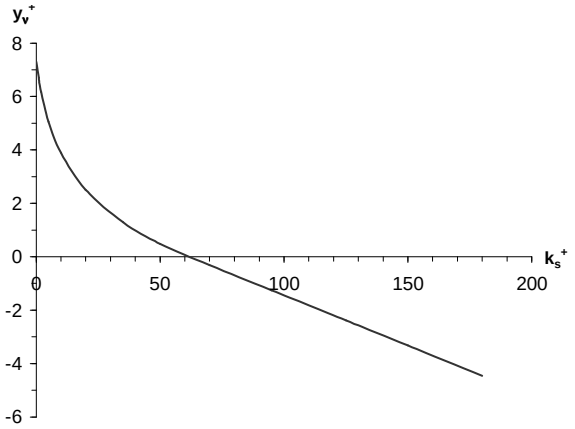

Figure 2: Zero-eddy-viscosity height as a function of relative roughness.

Dissipation

The turbulent-kinetic-energy equation requires *cell-averaged* production and dissipation. With the assumed eddy-viscosity profile (3) the cell-averaged production is

$$\begin{aligned} P_{av}^{(k)} &\equiv \frac{1}{\Delta} \int_0^\Delta \nu_\tau \left(\frac{\partial U}{\partial y}\right)^2 \mathrm{d}y \\ &= \frac{(\tau_w/\rho)^2}{\kappa \tilde{u}_\tau \Delta} \left\{ \ln \frac{\Delta^+ - y_v^+ + 1/\kappa}{y_{v0}^+ - y_v^+ + 1/\kappa} + \frac{1}{s_2} - \frac{1}{s_1} \right\} \end{aligned} \tag{12}$$

where

$$\begin{aligned} s_2 &= 1 + \kappa(\Delta^+ - y_v^+) \\ s_1 &= 1 + \kappa(y_{v0}^+ - y_v^+) \end{aligned} \tag{13}$$

whilst, with the dissipation profile (4), the cell-averaged dissipation is

$$\varepsilon_{av} = \frac{1}{\Delta} \int_0^\Delta \varepsilon \ \mathrm{d}y = \frac{\tilde{u}_\tau^3}{\kappa \Delta} \left\{ \ln \frac{\Delta^+ - y_d^+}{y_\varepsilon^+ - y_d^+} + \frac{y_\varepsilon^+}{y_\varepsilon^+ - y_d^+} \right\} \tag{14}$$

The values of y_d and y_ε in the dissipation profile (4) are found by matching the leading-order terms in the cell-averaged expressions (12) and (14). (Otherwise, $\tilde{u}_\tau$ is found to deviate significantly from u_τ in equilibrium boundary layers, negating a major assumption of the wall function). The result is that y_d and y_ε vary with roughness through y_v:

$$y_d^+ = y_v^+ - \frac{1}{\kappa} \tag{15}$$

$$y_\varepsilon^+ = y_d^+ + \frac{s_1}{\kappa} \exp\left(\frac{y_\varepsilon^+}{y_\varepsilon^+ - y_d^+} + \frac{1}{s_1}\right) \tag{16}$$

For arbitrary roughness, equation (16) must be solved iteratively. However, it converges very rapidly starting from the smooth-wall values

$$y_d^+ = 4.9, \qquad y_\varepsilon^+ = 27.4, \qquad \text{(smooth wall)} \tag{17}$$

In the dissipation equation, (4) is used to set the value of ε at the near-wall node as a boundary condition.

Stress-Transport Equations

The wall function can also be used for differential stress models, with cell-averaged production and dissipation used in the transport equations for the stresses. The production terms are first evaluated in local wall-tangential coordinates and then rotated to the fixed Cartesian system. In simple shear only the streamwise-normal-stress and shear-stress production terms are non-zero, and these are proportional to the production of turbulent kinetic energy:

$$\begin{aligned} P_{tt} &= -2\overline{u_t u_n}\frac{\partial U_t}{\partial n} &&= 2P^{(k)} \\ P_{tn} &= -\overline{u_n^2}\frac{\partial U_t}{\partial n} &&= \frac{\overline{u_n^2}}{\overline{u_t u_n}}P^{(k)} \end{aligned} \tag{18}$$

The ratio $\overline{u_n^2}/\overline{u_t u_n}$ can be specified directly, or taken from equilibrium values of the structure functions; (a value of –0.83 was used here).

Application to Rough-Walled Pipe Flow

Figure 3 shows predictions of friction factor in fully-developed pipe flow for various values of relative roughness with both 2-equation and differential stress models.

(a) Standard *k*-ε model

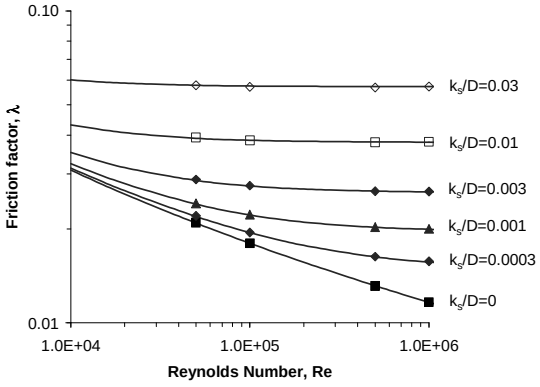

(b) Differential stress model (Launder et al., 1975)

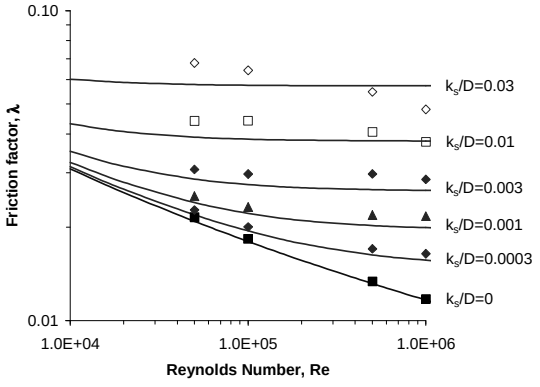

Figure 3: Friction factor in rough-walled pipe flow

SEDIMENT TRANSPORT AND MORPHODYNAMICS

Morphodynamics Equation

The movement of sediment by fluids is effected by either *suspended load* or *bed load*, with the latter dominating for larger sediments. Bed-load transport is largely determined by the bed shear stress, a crucial output of the wall function.

Sediment morphology is a dynamic process, whereby net accretion or depletion arises from an imbalance between the rates at which sediment enters and leaves a region. Conservation of sediment yields an integral equation for the average bed height z_b on each bed cell face (Figure 4):

$$(1-p)A_h\frac{\partial z_b}{\partial t} = -\oint_{\partial A}\mathbf{q}_b \bullet \mathrm{d}\mathbf{s} \wedge \mathbf{n} \tag{19}$$

A_h is the projected horizontal area and p is the porosity. $\mathbf{q}_b$ is the sediment flux (rate of transport of sediment per unit length of surface) and **n** is a unit vector normal to the bed.

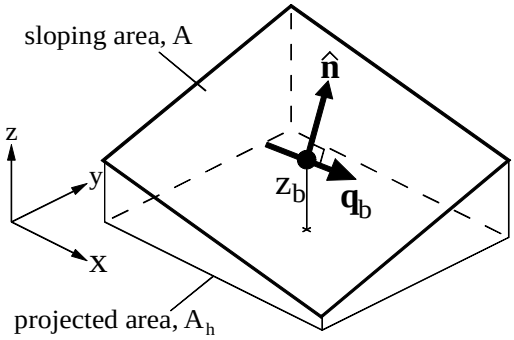

Figure 4. Sediment cell face

Sediment-Transport Formulae

For non-cohesive sediment, dimensional analysis leads to a dimensionless relationship between dimensionless bed flux, shear stress and particle diameter of the form

$$q^* = f(\tau^*, d^*) \tag{20}$$

where:

$$q^* = \frac{q_b}{\sqrt{(s-1)gd^3}} \tag{21}$$

$$\tau^* = \frac{\tau_w}{\rho(s-1)gd} \tag{22}$$

$$d^* = d\left[\frac{(s-1)g}{\nu^2}\right]^{1/3} \tag{23}$$

$s = \rho_s/\rho$ is the relative density of the sediment and d is the particle diameter. Popular models of this form include:

$$q^* = \frac{0.053}{d^{*0.3}}\left(\frac{\tau^*}{\tau^*_{crit}}-1\right)^{2.1} \quad \text{(Van Rijn, 1984)}$$

$$q^* = 8(\tau^* - \tau^*_{crit})^{3/2} \quad \text{(Meyer-Peter and Müller, 1948)} \tag{24}$$

with motion only if the bed stress exceeds a critical value τ^*_{crit}, which is a function of d^*.

Modifications for Large Slopes

Most bed-load sediment-transport formulae are used in conjunction with depth-averaged flow solvers and are designed for rivers or seabeds of very low slope. Recent work (Apsley and Stansby, 2007) suggests changes to predict sediment transport and morphology with large slopes. The important elements are:

1. Replacement of τ^* in the sediment-transport formulae by an *effective* stress formed by combining fluid stress with the downslope component of weight (Figure 5)
$$\boldsymbol{\tau}_{eff} A = \boldsymbol{\tau}_w A + (\rho_s - \rho) V g \sin\beta \mathbf{b} \quad (25)$$
Dividing by $(\rho_s - \rho) g d A$ this gives, in non-dimensional form:
$$\boldsymbol{\tau}^*_{eff} = \boldsymbol{\tau}^* + D_0 \sin\beta \mathbf{b} \quad (26)$$
where **b** is a unit vector down the line of maximum slope, β is the angle to the horizontal and the sediment-dependent parameter D_0 is determined by assuming incipient motion at the angle of repose. Since the downslope part is proportional to $-\nabla z_b$ this gives a diffusion-like component which aids the stability of the morphodynamics equation.

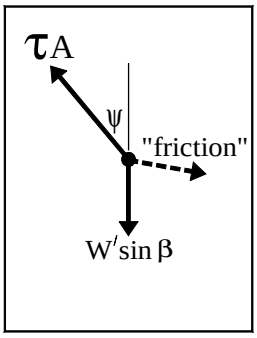

Figure 5. In-slope forces on sediment particles

2. Reduction of the critical effective stress in proportion to the slope-normal component of gravity:
$$\tau^*_{eff,crit} = \tau^*_{crit,0} \cos\beta \quad (27)$$
3. A simple *avalanche* model to redistribute material if the slope at any stage exceeds the angle of repose ϕ (Figure 6):
$$q_{aval} = (1-p) \frac{\frac{1}{2} L^2 (\tan\beta - \tan\phi)}{\cos\beta \, \Delta t} \quad (28)$$
4. A full 3-d evaluation of the integral sediment flux as in (19). (Most sediment-transport prediction is done using depth-averaged codes and ignores local surface orientation).
5. Two smoothing algorithms: the first of which treats the gradient-dependent part of the sediment flux in a manner akin to Rhie-Chow smoothing for mass-flux interpolation, and the second which suppresses variations in the signed difference between cell-face centroids and the control points used to define the bed (Figure 7) – this opposes changes in curvature.

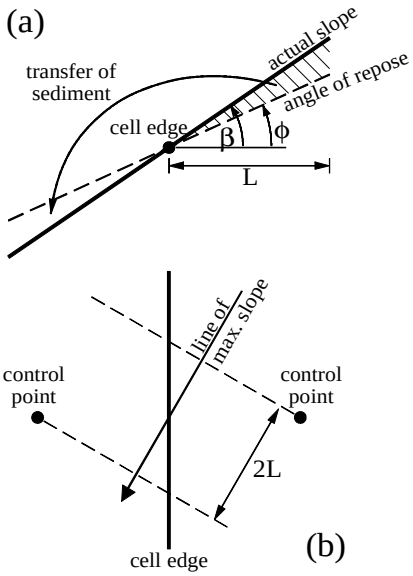

Figure 6. Redistribution of material in avalanche model.

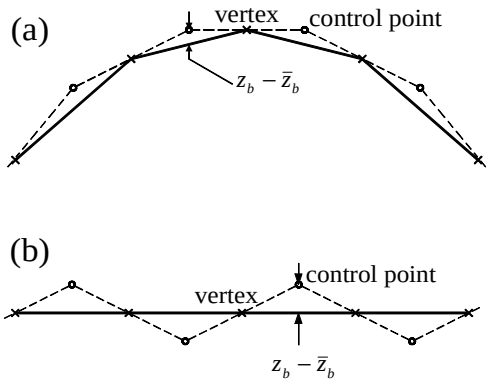

Figure 7. Using the difference between control points and face centroids to identify surface "wiggles".

APPLICATIONS

Scour and Accretion in a 90° Channel Bend

Kawai and Julien (1996) reported experimental measurements of bed scour in a 90° channel bend (channel width 0.2 m; centreline radius 0.6 m; longitudinal slope 1/300; normal depth 0.041 m, sand-grain size 0.6 mm). A steady flow of water (Q = 4 L s^{-1}) and sediment discharge (Q_s = 1.44 cm^3 s^{-1}) were maintained for 200 minutes, after which the channel bed was observed to have reached a quasi-steady state. During the experiment secondary currents in the bend (outward flow at the free surface, inward flow at the bed) led to substantial scour on the outside of the bend and deposition on the inside.

A time-dependent, surface-conforming, moving-grid simulation was conducted with a mesh of 90×20×12 cells. Flow calculations were undertaken with the standard k-ε model, whilst the Van Rijn (1984) model (modified as above for slopes) was used for sediment transport.

(a) Bed morphology

(b) Free-surface flow pattern

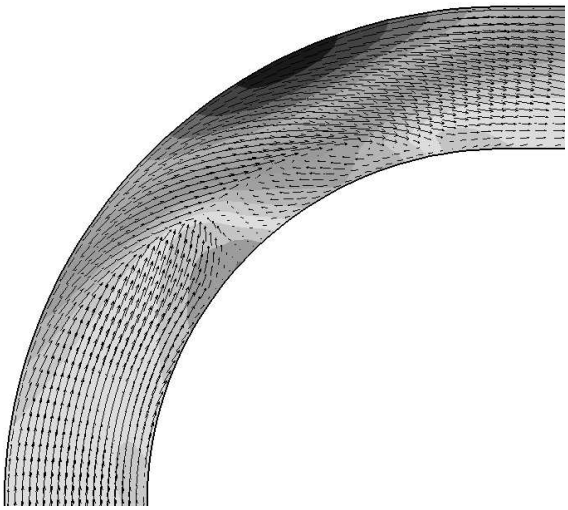

Figure 8: Morphology and flow pattern in a channel bend.

Figure 8 shows the computed bed profile and free-surface flow pattern. The maximum scour depth is nearly 3 times the original water depth and a point-bar deposit is formed on the inside of the bend.

Figure 9 shows computed and measured bed and free-surface heights along the channel banks, whilst Figure 10 shows the evolving bed and free-surface profiles at stations 30°, 40° and 60° around the bend.

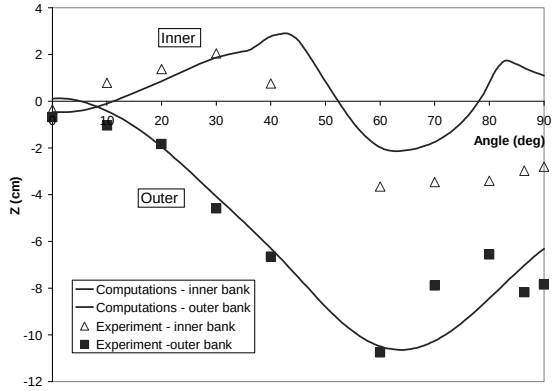

Figure 9: Bed morphology and free-surface flow in a channel bend.

30°

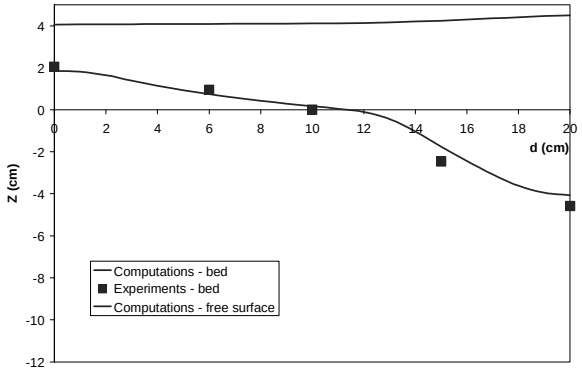

40°

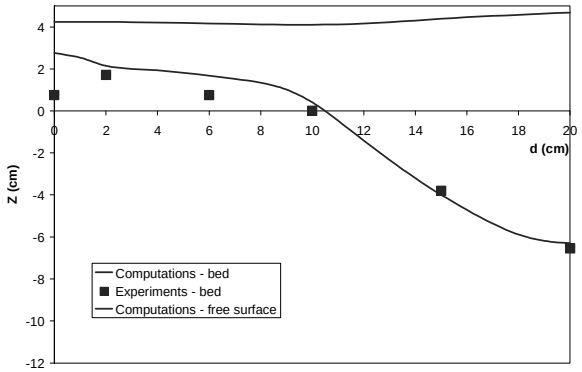

60°

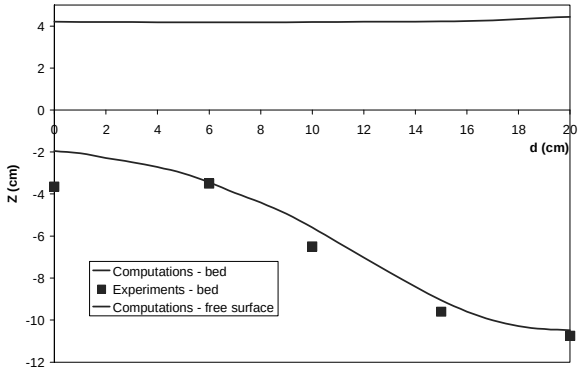

Figure 10: Bed and free-surface profiles in channel bend.

Evolution of Sand Mounds

Experiments were undertaken at HR Wallingford to study the evolution of sand mounds in both tidal and constant-current flow and on both mobile and non-mobile beds. Two initial sand-mound shapes have been simulated: a circular cone and an axisymmetric Gaussian hump. Simulations of the constant-current cases are shown here. Downstream separation and recirculation is a major feature, with interaction between the complex 3-d flow and the

morphodynamics. The grade of sediment (d_{50} = 454 μm; ρ_s = 2650 kg m^{-3}) is such that sediment transport is almost entirely bed load, with d^* = 11.5 and $\tau^*_{crit,0} = 0.032$.

Figure 11 shows the development of an initially conical sand mound, computed with the Meyer-Peter and Müller sediment-transport model. In a constant current and on a non-erodible bed this moves downstream, forming the characteristic shape of barchan sand dunes.

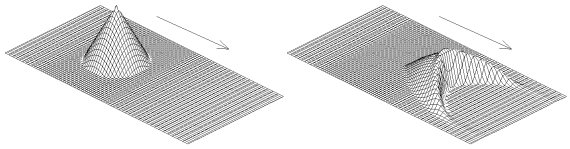

Figure 11: Evolution of a conical sand mound

Figure 12 shows the evolution of an initially Gaussian sand mound, demonstrating the difference between erodible and non-erodible beds. In the latter case the downstream recirculation results in the generation of deep scour holes, whilst at the upstream foot there is net accretion. A hydraulic jump is formed over the summit of the mound.

(a) Non-mobile bed

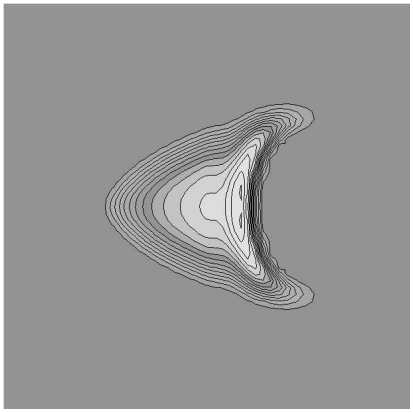

(b) Mobile bed

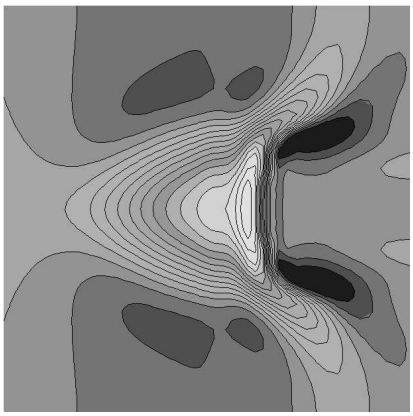

Figure 12: Development of a Gaussian sand mound; flow from left to right.

CONCLUSIONS AND FURTHER WORK

A novel wall function is described, which is suitable for arbitrarily rough surfaces. The velocity/shear-stress relationship is based on an assumed eddy-viscosity profile, with the zero-eddy-viscosity height and parameters in the dissipation profile being functions of roughness. These functional relationships are determined by enforcing strong asymptotic consistency with the log law.

Development of the wall function was motivated by sediment-transport applications. This led to further CFD developments for sediment transport and morphology with large slopes. Applications including steady flow in a channel bend and transient evolution of sand mounds are described here.

Future work will examine the inclusion of strong pressure gradients (which cause a linear, and not-necessarily flow-aligned, variation of stress with height). Cases where the pressure gradient causes a mismatch between the directions of near-wall velocity and bed stress can have a deleterious effect on sediment-transport modelling.

REFERENCES

Apsley, D.D., 2007, "CFD calculation of turbulent flow with arbitrary wall roughness", Flow, Turbulence and Combustion, Vol. 78, pp. 153-175.

Apsley, D.D. and Stansby, P.K., 2007, "Bed-load sediment transport with large slopes: a complete formulation within a general-purpose RANS flow solver", submitted to ASCE Journal of Hydraulic Engineering.

Craft, T.J., Gant, S.E., Gerasimov, A.V., Iacovides, H. and Launder, B.E., 2006, "Development and application of wall-function treatments for turbulent forced and mixed convection flows", Fluid Dynamics Research, Vol. 38, pp. 127-144.

Launder, B.E., Reece, G.J. and Rodi, W., 1975, "Progress in the development of a Reynolds-stress turbulence closure", J. Fluid Mech., Vol. 68, pp. 537-566.

Meyer-Peter, E. and Müller, R, 1948, "Formulas for bed-load transport", Rept 2nd Meeting Int. Assoc. Hydraul. Struct. Res., Stockholm, 39-64.

Suga, K., Craft, T.J and Iacovides, H., 2006, "An analytical wall-function for turbulent flows and hear transfer over rough walls". International Journal of Heat and Fluid Flow, Vol. 27, pp 852-866.

Van Rijn, L.C., 1984, "Sediment transport, Part I: Bed load transport", ASCE J. Hydraulic Engineering, Vol. 110, pp. 1431-1456.